

Dual-Functional Ca-Ion-Doped Layered δ -MnO₂ Cathode for High-Performance Aqueous Zinc-Ion Batteries

Dongmei Xie, Yan Wang, Leiwu Tian, Haiji Huang, Jianyang Sun, Dong-Won Kim,*
Jiachang Zhao,* and Jianfeng Mao*

Aqueous zinc-ion batteries (ZIBs) have gained significant attention owing to their high energy densities, low costs, and enhanced safety profiles. However, the development of suitable host materials (i.e., cathodes) with high capacity, structural stability, and rate performance remains challenging. Herein, a nanoflower-like Ca_{0.10}MnO₂·0.61H₂O (CaMnO) is successfully synthesized as a high-performance cathode material for ZIBs using a simplified one-step hydrothermal method. The unique nanoflower-like 3D porous structure provides a continuous conductive path and abundant adsorption sites for Zn²⁺ ions and mitigates aggregation during long-term cycling processes. In addition, doping Ca²⁺ ions into the interlayer of MnO₂ has a dual functional effect: 1) it acts as a pillar to broaden the interlayer spacing and enhance the crystal structure stability, and 2) it induces the formation of oxygen vacancies to enhance the reaction kinetics and increase the reversible capacity. Therefore, the CaMnO cathode exhibits a high specific capacity of 289 mAh g⁻¹, with excellent capacity retention (90%) over 750 cycles at a high current rate of 1.5 A g⁻¹. This study provides a new perspective on the development of advanced cathode materials for ZIBs.

energy storage technologies owing to their high energy density, low production cost, and simple fabrication processes.^[2] More importantly, aqueous ZIBs that use water as the solvent can effectively reduce the risk of thermal runaway and ensure intrinsic safety.^[3] However, the main obstacle to the industrialization of aqueous ZIBs is the development of suitable host materials (i.e., cathodes) to accommodate the reversible insertion/extraction of Zn²⁺ ions with large ionic radii over extended cycling periods.^[4] To date, a diverse range of materials has been reported for use as cathodes in ZIBs, including Prussian blue analogs, Mn-based oxides, V-based compounds, and polyanionic compounds.^[3,5] Among these, Mn-based oxides are considered the most promising cathode materials because of their diverse synthesis routes and crystal structures, low cost, nontoxicity, and environmental benignity.^[6] However, the large-scale application of Mn-based cathodes faces two main challenges: 1) phase

1. Introduction

The development of advanced electrochemical energy storage devices is of considerable significance for solving energy crises and environmental pollution problems.^[1] Aqueous zinc-ion batteries (ZIBs) are expected to become the next generation of large-scale

transitions during electrochemical processes, which may lead to anisotropic changes in lattice parameters and the formation of microcracks, and 2) the disproportionation of Mn³⁺ (2Mn³⁺ → Mn²⁺ + Mn⁴⁺), which results in the dissolution of active materials.^[7–9] To this end, researchers have developed various modification strategies to enhance the electrochemical performance of cathode materials for aqueous ZIBs.

MnO₂ has been widely investigated owing to its higher specific capacity (310 mAh g⁻¹), higher operating voltage (1.0–1.8 V versus Zn²⁺/Zn), and various crystallographic polymorphisms (e.g., α -, β -, γ -, δ -, λ -, and ϵ -type structures).^[10] In particular, layered δ -MnO₂ with large ionic diffusion channels (≈ 0.7 Å) exhibits a rapid and reversible (de)intercalation reaction with Zn ions.^[11] Unfortunately, similar to other Mn-based oxides, δ -MnO₂ exhibits significant capacity degradation and poor rate capability in ZIB systems.^[12] The inferior electrochemical performance is related not only to the complex phase transition and dissolution of Mn but also to the sluggish diffusion kinetics and strong electrostatic interaction between Zn²⁺ and the host material, which hinders the potential of using Mn-based oxides as cathodes for ZIBs.^[13] Therefore, various strategies, such as morphological control, surface modification, defect engineering, and doping modification, have been proposed to achieve Mn-based oxides as feasible cathode materials for ZIBs.^[14] Surface

D. Xie, L. Tian, D.-W. Kim
Department of Chemical Engineering
Hanyang University
Seoul 04763, South Korea
E-mail: dongwonkim@hanyang.ac.kr

D. Xie, Y. Wang, H. Huang, J. Sun, J. Zhao
College of Chemistry and Chemical Engineering
Shanghai University of Engineering Science
Shanghai 201620, P. R. China
E-mail: zjc@sues.edu.cn

J. Mao
School of Chemical Engineering
The University of Adelaide
Adelaide, SA 5005, Australia
E-mail: jianfeng.mao@adelaide.edu.au

The ORCID identification number(s) for the author(s) of this article can be found under <https://doi.org/10.1002/adfm.202413993>

DOI: 10.1002/adfm.202413993

coating and morphology control strategies enhance the Zn storage performance of cathodes by improving electron/ion diffusion and mitigating volume expansion during electrochemical processes.^[15,16] Through the efforts of researchers, several aqueous ZIB systems with advanced electrochemical performances have been proposed in recent years.^[17,18] However, the inherent low electron/ion conductivity of layered oxide cathode materials results in low reaction kinetics and poor cycling stability at high current rates, which poses a bottleneck for the application of microstructure enhancement strategies.^[19] The structural engineering strategy of doping and surface chemical control, which can fundamentally improve the reaction kinetics of the cathode, is considered a feasible solution for enhancing the electrochemical performance of ZIBs.

Functional defect engineering improves the electrochemical performance of active materials by endowing them with new electronic properties and adjusting their surface chemical properties, which has attracted the attention of researchers.^[20–22] As the most important type of defect in oxide materials, oxygen vacancies can regulate the electron density by redistributing the local charge states of the transition metal layers.^[19] This regulation decreases the reaction energy barrier of the active material by adjusting the bandgap, thereby fundamentally improving the reaction kinetics and ion diffusion efficiency of MnO₂.^[23] In addition, abundant oxygen vacancies can act as electrochemically active sites, facilitating redox reactions between the electrolyte and cathode, thereby effectively improving the charge storage capacity of oxide materials. For example, Wang's group synthesized MnO₂ with oxygen vacancies using a three-step method, achieving a high energy density of 40.2 Wh kg⁻¹ and a maximum power density of 22.28 kW kg⁻¹.^[24] Han et al. developed a β-MnO₂ cathode with oxygen defects by leveraging the reducing property of NaBH₄, achieving a high capacity retention of 94% after 300 cycles at 500 mA g⁻¹.^[25] Similarly, Li et al. introduced abundant oxygen vacancies into δ-MnO₂ using a KBH₄ reduction treatment, which significantly enhanced the reversible capacity (551.8 mAh g⁻¹) and extended the cycle life (90% capacity retention after 500 cycles at 3 A g⁻¹).^[26] Lu's group extracted oxygen anions from the ZnMn₂O₄ cathode through low-temperature H₂ reduction, achieving a high capacity retention of 93.8% after 300 cycles at 8 mA cm⁻².^[27] Chen et al. prepared an oxygen-rich vacancy Zn-MnO₂ cathode using plasma treatment technology to optimize the electronic structure and enhance electrochemical performance, achieving a long cycle life of 1000 cycles at 3 A g⁻¹.^[28] Although the modified cathode demonstrates excellent Zn storage performance, introducing oxygen vacancies often involves complex post-treatment processes, which increases the production costs and is not conducive for the commercial application of aqueous ZIBs. According to previous reports, non-equilibrium cation doping can significantly reduce the formation energy of oxygen vacancies, thereby introducing abundant oxygen vacancies into the bulk materials.^[11,29,30] In addition, dopants incorporated into the crystal structure or interlayer spacing can act as pillars to suppress interlayer sliding and structural collapse while releasing the electrochemically active potential of the oxide cathode.^[31] Therefore, to improve the stability of the layered framework and induce the formation of oxygen vacancies, divalent Ca ions with intercalation effects are preferred as suitable dopants.^[32]

Hence, this study proposes a one-step hydrothermal method for synthesizing nanoflower-like δ-MnO₂ cathodes to reduce agglomeration during cycling and further improve structural stability by introducing Ca²⁺ as a stabilizer. First, the porous nanostructure shortens the diffusion distance of Zn²⁺ and provides more reaction sites. In addition, ex situ X-ray diffraction (XRD) and X-ray photoelectron spectroscopy (XPS) results revealed that the introduced Ca²⁺ ions have dual functional effects: 1) they act as pillars to improve the stability of the layered framework structure and alleviate changes in crystal parameters; 2) they induce the formation of abundant oxygen vacancies to increase the number of reaction sites, enhance reaction kinetics, and fundamentally improve the Zn storage behavior of oxide materials. Hence, the optimized cathode (Ca_{0.10}MnO₂·0.61H₂O) exhibits a high reversible capacity (290 mAh g⁻¹) and long cycling life (80% capacity retention after 1000 cycles at 1.5 A g⁻¹). This study provides a simple and feasible solution to promote the development of advanced cathode materials for aqueous ZIBs.

2. Results and Discussion

As shown in **Figure 1**, δ-MnO₂ and Ca²⁺ doped δ-MnO₂ (CaMnO) samples were synthesized through a simple one-step hydrothermal method. It is proposed to stabilize the layered framework structure and increase the interlayer spacing through a chemical pre-intercalation (Ca-doping) process, thereby improving cycling stability and rate performance.^[33–35] **Figures 2a–c** and **S1a,b** (Supporting Information) depict the scanning electron microscopy (SEM) images of CaMnO and δ-MnO₂ at different magnifications, which show that both CaMnO and δ-MnO₂ samples present a 3D flower-like porous nanostructure composed of 200 nm nanosheets. This structure can alleviate the volume changes in the lattice parameters during the Zn-ion insertion/extraction processes, which play a key role in enhancing the structural stability of the oxide cathode. Compared with δ-MnO₂, the microspheres of CaMnO are uniformly dispersed without apparent aggregation, indicating that the introduction of Ca²⁺ ions is beneficial for maintaining the framework structure and providing a suitable host for the insertion of Zn²⁺ ions. The Brunauer–Emmett–Teller measurements of the prepared samples are shown in **Figure S2** (Supporting Information). As expected, CaMnO with less aggregation shows a larger specific surface area (32.5 m² g⁻¹) compared with δ-MnO₂ (14.2 m² g⁻¹), providing more active sites for electrochemical reactions. This 3D porous nanostructure was beneficial for accelerating electron migration and ensuring the diffusion kinetics of H⁺/Zn²⁺, thereby providing a high rate capability. The microstructures of the prepared samples were measured using transmission electron microscopy (TEM) analysis (**Figure 2d**; **Figure S1c**, Supporting Information). CaMnO was assembled from nanosheets with diameters of ≈200 nm, which is consistent with the SEM results. **Figure S1d** (Supporting Information) shows the HR-TEM image of δ-MnO₂, where a lattice spacing of 0.723 nm can be observed, indicating the typical (001) crystal plane of layered MnO₂.^[26] It is evident that the interlayer spacing of the (001) plane in the Ca-doped sample has increased to 0.749 nm (**Figure 2e**), indicating that the intercalation effect of hydrated Ca²⁺ ions expands the ion diffusion channel, thereby enhancing ion diffusion kinetics. The corresponding selected-area electron diffraction (SAED)

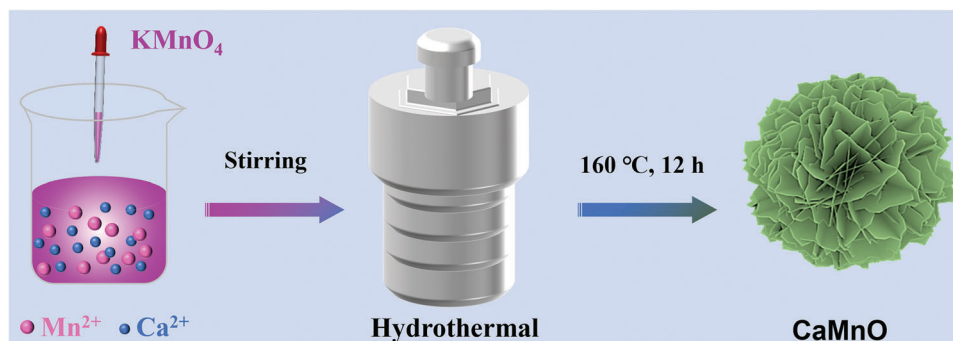


Figure 1. Schematic for the synthesis of CaMnO.

patterns of CaMnO (inset in Figure 2e) display two polycrystalline rings indexed to the (001) and (002) planes of layered MnO_2 , indicating that the resulting cathode had a monoclinic structure. The energy-dispersive spectroscopy (EDS) of CaMnO suggests that the Ca, Mn, and O species are uniformly distributed in the nanosheets, highlighting the consistency of the synthesized cathode (Figure 2f). Therefore, the microscopic morphology analysis proves that the prepared CaMnO cathode has a unique nanoflower-like structure, which is expected to achieve high rate capability and long-term cycling stability.

The crystal structures of the synthesized cathodes were determined using X-ray diffraction (XRD) analysis. As shown in Figure 3a, characteristic peaks belonging to the (001) and (002) planes were observed, and no impurity peaks were detected, indicating that MnO_2 and CaMnO with the same monoclinic structure were successfully prepared (JCPDS No. 80–1098; space group $C2/m$). Compared with $\delta\text{-MnO}_2$, the (001) peak of CaMnO gradually shifts toward a lower diffraction angle with increas-

ing Ca-doping concentration, which is related to the interlayer expansion caused by the intercalation effect of hydrated Ca^{2+} ions (Figure S3, Supporting Information). According to reports, the interlayer spacing of the layered cathode after chemical pre-intercalation treatment is proportional to the radius of hydrated ions, which is consistent with the experimental results, proving that the introduced Ca^{2+} ions preferentially insert into the interlayer.^[33] However, excessive Ca-doping leads to the formation of CaMn_2O_4 impurities, which significantly affect the electrochemical performance of the cathode. As shown in Figure S4 (Supporting Information), the optimal Ca-doped sample was identified through cycling stability tests. The results indicated that the sample with a CaCl_2 to MnSO_4 ratio of 1:1 exhibited the highest reversible capacity and excellent cycling stability. This suggests that the selected doping amount is close to the optimal value, allowing the cathode to maintain structural stability without sacrificing reversible capacity. Therefore, this sample was chosen as the focus of this study. The lattice parameters were

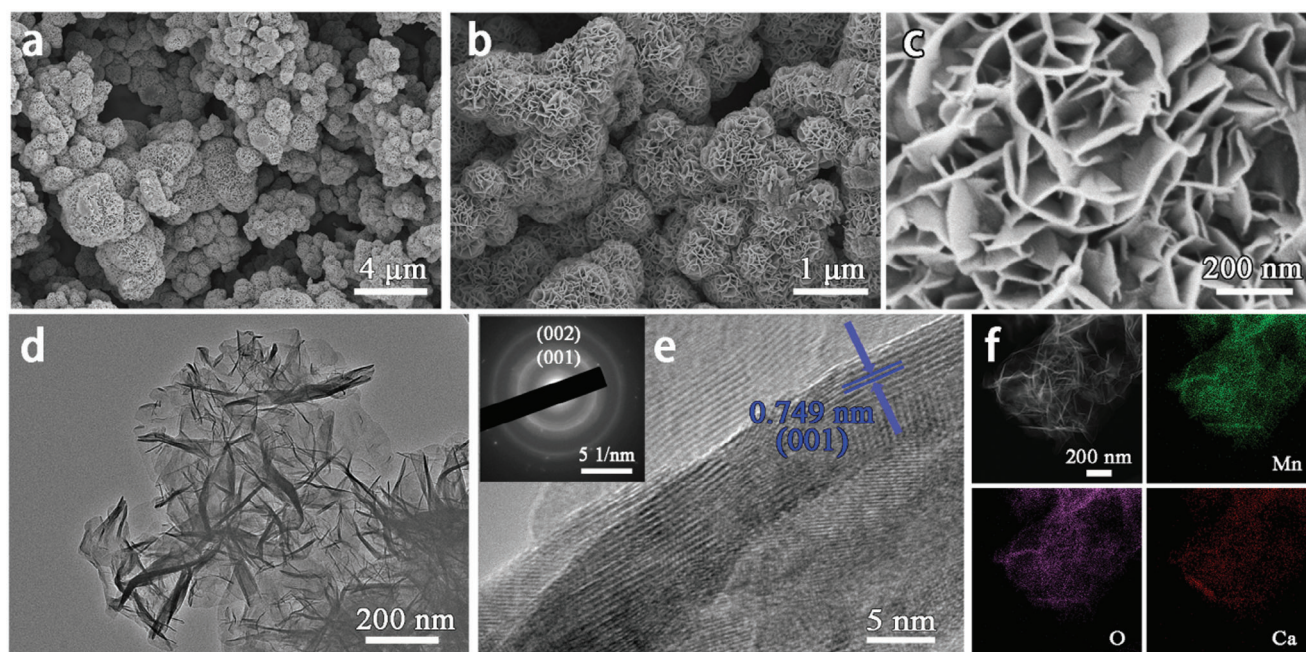


Figure 2. Morphology and structure of CaMnO. a–c) SEM images of CaMnO at different magnifications; d–e) TEM, HR-TEM, and SAED images of CaMnO; f) EDS images of CaMnO.

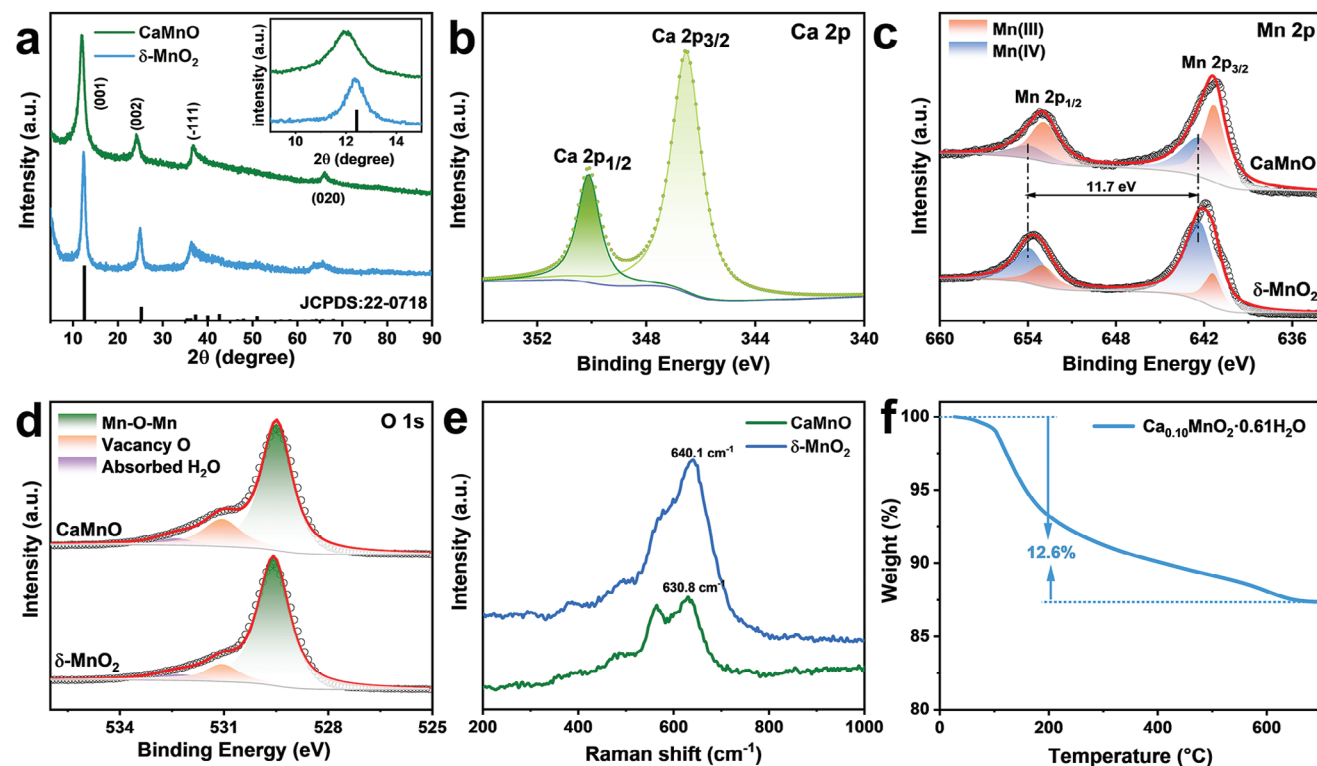


Figure 3. Material characterization of the prepared cathodes. a) XRD pattern and crystal structure illustration of CaMnO and δ -MnO₂; b) high-resolution XPS spectra of Ca 1s in CaMnO; high-resolution XPS spectra of (c) Mn 2p and (d) O 1s in CaMnO and δ -MnO₂; e) Raman spectra of CaMnO and δ -MnO₂; f) TGA curve of the as-prepared CaMnO sample from 30 to 800 °C.

calculated using the Rietveld refinement method based on the FullProf program (Figure S5, Supporting Information). The slight difference between the calculated results and the experimental mode indicated successful refinement (Table S1, Supporting Information). The results indicate that the introduction of Ca²⁺ ions increased the interlayer spacing from 7.23 to 7.36 Å, providing a wide diffusion channel for Zn ions and potentially achieving high rate capability.

The composition and chemical state of the synthesized cathode were further investigated using X-ray photoelectron spectroscopy (XPS). As shown in Figure 3b, the convolution peaks at 346.0 and 349.6 eV correspond to Ca 2p_{3/2} and Ca 2p_{1/2}, respectively.^[36] In addition, inductively coupled plasma-optical emission spectroscopy (ICP-OES) results confirmed that the atomic ratio of Ca to Mn was 0.10:1, which is consistent with the XPS results (0.13:1), demonstrating the successful synthesis of the designed doped cathode (CaMnO). The high-resolution XPS spectra of Mn indexed to Mn 2p_{3/2} and Mn 2p_{1/2} spin orbitals can be further deconvoluted into Mn (IV) (642.4, 654.1 eV) and Mn (III) (641.3, 653.0 eV), respectively (Figure 3c). The introduction of Ca ions leads to an increase in the integrated peak area of Mn³⁺/Mn⁴⁺ from 0.26 to 1.21 (the average oxidation state of Mn decreases from 3.79 to 3.45), which is related to the charge compensation and the formation of oxygen vacancies caused by Ca doping. The high-resolution XPS spectrum of O1s (Figure 3d) shows characteristic peaks corresponding to Mn–O–Mn bonds (529.6 eV), oxygen vacancies (531.1 eV), and absorbed water (532.3 eV), which is consistent with published

reports.^[26,37] CaMnO exhibits a higher peak intensity of oxygen vacancies, which further confirms the increase in oxygen vacancy concentration caused by Ca²⁺ doping. Electron paramagnetic resonance (EPR) measurements were performed on the prepared cathodes to provide fingerprint evidence of oxygen vacancies. As shown in Figure S6 (Supporting Information), CaMnO exhibits a relatively strong electron spin resonance (EPR) signal at $g = 2.001$, confirming the presence of oxygen vacancies.^[26] The Raman spectrum of the prepared cathodes are shown in Figure 3e, featuring characteristic peaks located at 625–645 and 575–585 cm⁻¹, respectively attributed to the symmetric stretching vibration ν_2 (Mn–O) of MnO₆ group and the ν_3 (Mn–O) stretching vibration in the [MnO₆] plane.^[38–40] For pure oxides with few defects, the band intensity ≈ 640 cm⁻¹ is particularly high, often overshadowing other characteristic peaks.^[38] In contrast, doped samples typically show a strong decrease in Raman intensity and more pronounced ν_3 (Mn–O) strain vibrations.^[41] This effect is associated with a high ratio of Mn(IV) in the birnessite family, a phenomenon frequently observed in previous reports.^[40,42] Compared with δ -MnO₂, the Raman bonds of CaMnO undergo a significant blue shift, which is related to the interlayer expansion caused by Ca²⁺ ions entering the interspace.^[43] In addition, the decrease in the Raman peaks of the Ca-doped samples is related to changes in the covalent interactions between the Mn and O layers after the formation of oxygen vacancies. These results indicate that Ca doping can induce the formation of oxygen vacancies, which play a crucial role in improving the ion/electron conductivity of the cathode. As shown in Figure 3f, thermogravimetric

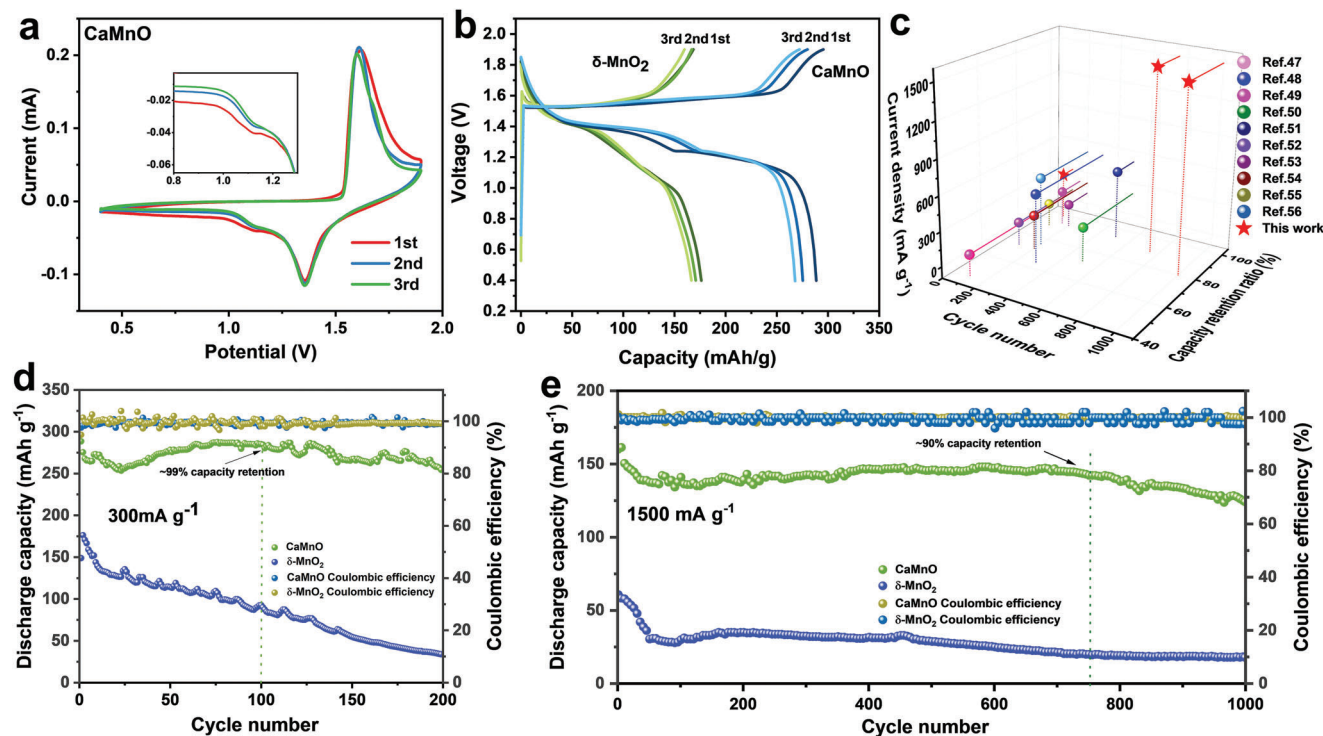


Figure 4. Electrochemical performance of the as-synthesized cathodes. a) CV curves of CaMnO at 0.1 mV s⁻¹; b) Charge–discharge curves of δ -MnO₂ and CaMnO at 300 mA g⁻¹; c) Comparison of cycling stability between CaMnO and other cathode materials previously reported; Cycling performance of δ -MnO₂ and CaMnO at the current densities of (d) 300 mA g⁻¹ and (e) 1500 mA g⁻¹.

analysis (TGA) revealed that the crystalline water content of CaMnO was $\approx 12.6\%$. Combining the XPS and ICP analysis results, the accurate molecular formula of CaMnO can be defined as Ca_{0.10}MnO₂·0.61H₂O.

To verify the effect of Ca²⁺ doping on the Zn²⁺ storage performance, galvanostatic charge–discharge and cyclic voltammetry (CV) tests were conducted at a voltage window of 0.4 and 1.9 V. Considering the crucial role of electrolytes and binders in the electrochemical performance of ZIBs, the influence of different components on the cycling stability of the cathode was investigated (Figures S7 and S8, Supporting Information). For the modified binder (Ca-SA), the strong binding between Ca²⁺ and sodium alginate effectively prevents the dissolution of Mn, while also improving the mechanical stability and hydrophilicity of the active materials (Figure S8, Supporting Information). Compared to traditional inorganic salt systems (ZnSO₄/MnSO₄), Zn(CF₃SO₃)₂, with its larger anion radius, reduces the number of water molecules surrounding Zn²⁺ cations and diminishes the solvation effect.^[14] Consequently, the introduction of anions with large ionic radii facilitates Zn²⁺ transport, improves charge transfer, and enhances ionic conductivity. Notably, the introduction of Mn²⁺ additives enhances the cycling stability and reversible capacity of the cathode material through the reversible electro-deposition/dissolution process of MnO_x on the cathode surface.^[44] As shown in Figure S7a (Supporting Information), the cell using an electrolyte containing Mn²⁺ additives exhibited a gradual increase in capacity during the first 100 cycles. However, this deposition and stripping behavior may lead to dendrite formation and structural damage, causing a significant drop in

capacity after 100 cycles. In contrast, cells using Zn(CF₃SO₃)₂ electrolyte are able to maintain long-term cycling stability, even at high current densities of 1.5 A g⁻¹. Similarly, the cell using 3 M Zn(CF₃SO₃)₂/0.2 M Mn(CF₃SO₃)₂ electrolyte showed relatively good cycling stability but still exhibited significant capacity degradation during prolonged cycling (Figure S7b, Supporting Information). Therefore, the modified binder (Ca-SA) and electrolyte (3 M Zn(CF₃SO₃)₂) were used in subsequent experiments. As shown in Figures 4a and S8a (Supporting Information), the two samples exhibit similar CV curves. The reduction peaks at 1.1 and 1.38 V correspond to the insertion reactions of H⁺ and Zn²⁺ ions, respectively, accompanied by the reduction of Mn (from Mn⁴⁺ to Mn³⁺). The oxidation peak, located at ≈ 1.7 V, corresponds to the reverse process. It should be noted that modified electrolytes containing anions with a larger ionic radius can weaken the bonding strength between Zn ions and solvated H₂O, thereby reducing desolvation energy while synergistically promoting the intercalation of H⁺ and Zn²⁺ ions.^[45] As a result, batteries using modified electrolytes exhibit a weaker reduction peak at 1.1 V compared to those using conventional electrolytes.^[46] Furthermore, the Ca-doped cathode provides a large ion diffusion channel and high ion diffusion kinetics, thereby enhancing the synergistic intercalation of Zn²⁺ and H⁺ ions, resulting in a weaker reduction peak at 1.1 V (Figure 4a). Compared with δ -MnO₂, the overlap of the first three CV curves of CaMnO indicates the reversible insertion/extraction behavior of Zn²⁺ in 3D porous nanostructures, demonstrating its excellent structural stability. The charge/discharge curves of the synthesized cathodes at 300 mA g⁻¹ also show two discharge platforms (1.1 and

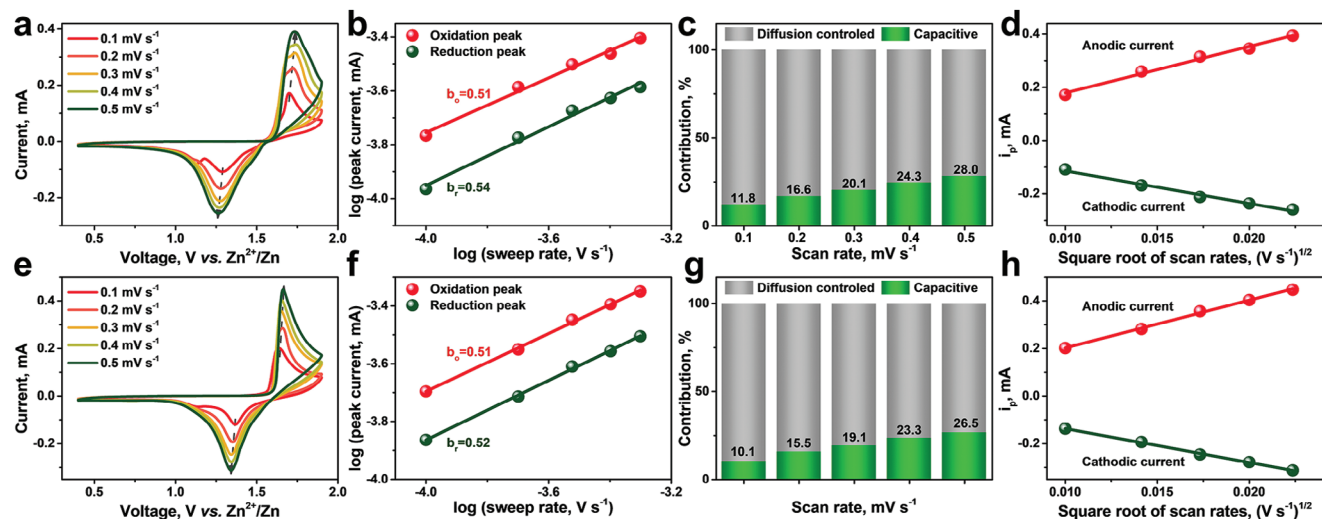


Figure 5. Electrode process kinetics of δ -MnO₂ and CaMnO. CV curves of the (a) δ -MnO₂ and (e) CaMnO electrodes at different scan rates, (b,f) log(peak current) versus log(sweep rate) plots of the oxidation and reduction peaks in the CV curves during cycling and (c, g) contribution ratios of the capacitance capacity and diffusion-controlled capacity in the (b, c) δ -MnO₂ and (f, g) CaMnO electrodes. A linear relationship between the peak current and the square root of the scanning rate for the (d) δ -MnO₂ and (h) CaMnO cathodes.

1.38 V), corresponding to the stepwise intercalation of H⁺/Zn²⁺ and the reduction of Mn⁴⁺, as well as a flat charging platform (1.7 V) corresponding to the reverse reaction (Figure 4b). This reflects the reversible intercalation of H⁺/Zn²⁺ ions, which is consistent with the CV results. CaMnO delivers a high initial reversible capacity of 289 mAh g⁻¹ with a low overpotential of 0.13 V at 300 mA g⁻¹, whereas δ -MnO₂ exhibits a low capacity (176 mA g⁻¹) and high polarization (0.24 V). The high reversible capacity and low overpotential of CaMnO indicate that the constructed porous network structure provided more Zn-ion active sites and fast ionic diffusion channels. The rate performance of the obtained cathode is shown in Figure S9 (Supporting Information), where CaMnO exhibits reversible capacities of 250.4, 193.1, 132.9, 103.5, 88.7, and 70.6 mAh g⁻¹ at the current densities of 0.5, 1, 1.5, 2, 3, and 4 A g⁻¹, respectively. Even at a high current density of 5 A g⁻¹, it still provides a specific capacity of 50.6 mAh g⁻¹ (corresponding to 20.4% of that at 0.1C). On the contrary, the original δ -MnO₂ shows a low capacity of 3.5 mAh g⁻¹ at a high current rate of 5 A g⁻¹, which indicates almost failure, demonstrating the excellent rate capability of CaMnO.

Figure 4d shows the cyclic stability of CaMnO and δ -MnO₂ at a current density of 300 mAh g⁻¹. CaMnO maintained a high discharge capacity of 260 mAh g⁻¹ after 100 cycles, with a high capacity retention of 99%. This is much higher than that of pure δ -MnO₂ (with a residual capacity of 34 mAh g⁻¹ and a capacity retention of 22%), indicating that the structural integrity was effectively improved after Ca²⁺ doping. Even at a high-current density of 1500 mA g⁻¹, CaMnO maintained a high reversible capacity of 140 mA g⁻¹ after 750 cycles (90% capacity retention) and 124 mA g⁻¹ after 1000 cycles (80% capacity retention) (Figure 4e). On the contrary, δ -MnO₂ could not withstand such a high current rate, and hence, it could only provide a poor capacity of 17 mA g⁻¹ after 1000 cycles. More importantly, the electrochemical performance of CaMnO was significantly superior to that of other reported cathodes (Figure 4c; Table S2, Supporting Information).^[47–56] The improved cyclic stability is related to the introduction of Ca²⁺

ions, which can prevent structural collapse, enhance structural stability, and inhibit the dissolution of Mn during the repeated insertion/extraction of Zn ions. Additionally, an increase in the concentration of oxygen vacancies enhances electronic conductivity and provides sufficient electroactive sites to increase the reversible capacity of the resulting cathode. Therefore, CaMnO exhibits a superior electrochemical performance than δ -MnO₂ in aqueous ZIBs. To demonstrate the practicality of the constructed cathode, it was assembled into a full cell by coupling with pre-zincified activated carbon cloth (ACC),^[57] rather than using Zn foil. As shown in Figure S10 (Supporting Information), the CaMnO//ACC full cell exhibits excellent cycling stability at 300 mA g⁻¹, retaining 84.3% of its initial capacity after 150 cycles. Although the cycling stability of the full cell is lower compared to the half-cell, this may be attributed to the structural instability of the ACC anode, which will require further optimization in the future.^[58]

To test the electrode process kinetics of δ -MnO₂ and CaMnO, the cathodes were characterized through CV testing (from 0.1 to 0.5 mV s⁻¹). As shown in Figure 5e, the shape and peak position of the CV curve of CaMnO did not significantly deviate with increasing scanning rate, indicating a high-rate Zn-ion insertion/extraction reaction. However, the cathodic peak in the CV curves of δ -MnO₂ (Figure 5a) shifts toward a lower potential, whereas the anodic peak shifts toward a higher potential, indicating a significant increase in polarization. The charge storage mechanism of the cathodes can be evaluated by the relationship between the scanning rate (v) and peak current (i): $i = av^b$, where $b = 0.5$ represents a diffusion-controlled electrochemical process, and $b = 1$ indicates a capacitive process.^[59] As shown in Figure 5f, the b values corresponding to the anode/cathode peaks of CaMnO are 0.52 and 0.51, respectively, indicating that ionic diffusion limits the reaction rate. According to Dunn's method,^[60] the corresponding proportions of two different capacitors can be evaluated as $i = k_1v + k_2v^{1/2}$, where k_2 and k_1 represent the coefficients of diffusion and capacitance contribution, respectively. The

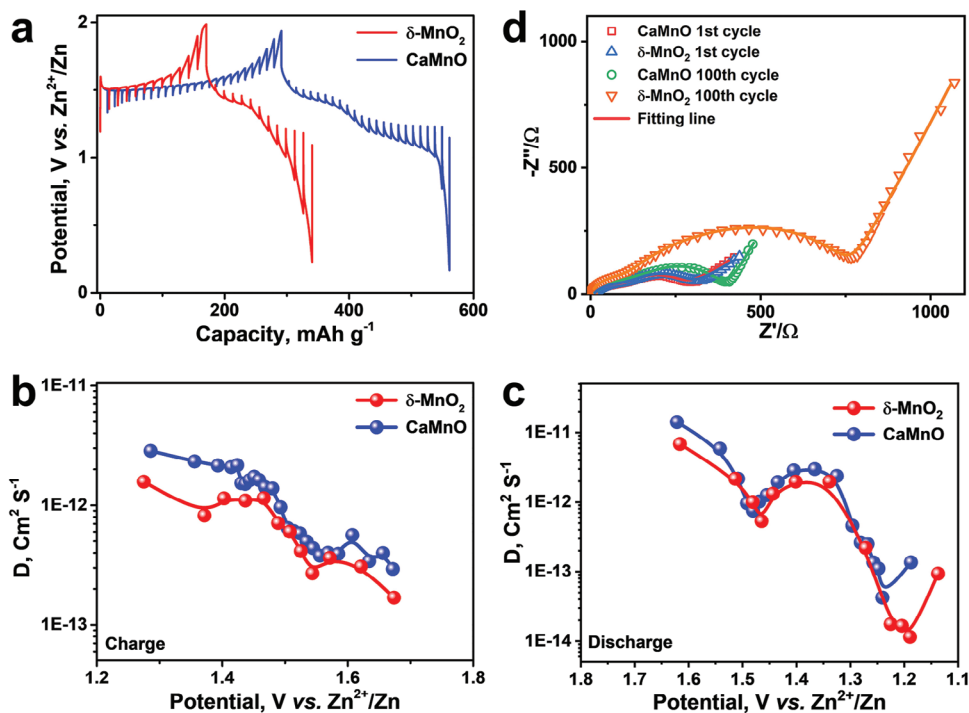


Figure 6. Reaction kinetics of the prepared cathode. a) Discharge/charge curves in the GITT measurement of CaMnO and the corresponding diffusivity coefficient. b,c) Ion diffusion coefficients of the CaMnO and $\delta\text{-MnO}_2$ cathodes during the charge and discharge process. d) Nyquist plots of the CaMnO and $\delta\text{-MnO}_2$ cathodes after the first and 100th cycles.

capacitive contribution of both cathodes increases with the scanning rate; however, even at a high scanning rate of 0.5 mV s^{-1} , CaMnO exhibits a capacitive contribution of only 26.5%, which is slightly lower than that of $\delta\text{-MnO}_2$ (28.0%). The relatively low capacitive contribution of both $\delta\text{-MnO}_2$ and CaMnO indicates that solid-state diffusion is the kinetic limiting step (Figure 5c,g). Therefore, the increase in the reversible capacity of CaMnO is not related to the enhanced surface-controlled capacitive resulting from an increased specific surface area. Instead, this is due to the formation of oxygen vacancies induced by Ca^{2+} ions, which provides more electrochemical active sites and improves ion diffusion kinetics. Although the capacitive contribution of CaMnO is slightly lower than that of the original sample, the electrochemical processes of both samples are primarily dominated by diffusion-controlled processes, making the reaction kinetics largely limited by ion diffusion ability.^[28] CaMnO with large interlayer spacing and abundant oxygen vacancies achieves high-rate performance by enhancing ion diffusion efficiency. The ionic diffusion coefficient (D) was calculated based on the Randles–Sevcik relationship, which is a linear fit of i and $v^{1/2}$ (Figure 5d,h). The average D value of CaMnO ($2.86 \times 10^{-10} \text{ cm}^2 \text{ s}^{-1}$) is higher than that of $\delta\text{-MnO}_2$ ($2.15 \times 10^{-10} \text{ cm}^2 \text{ s}^{-1}$), indicating that the increase in oxygen concentration effectively enhances the Zn-ion diffusion kinetics. The rapid Zn^{2+} diffusivity was related to the excellent rate performance of the CaMnO cathode.

The galvanostatic intermittent titration technique (GITT) and electrochemical impedance spectroscopy (EIS) analyses were conducted to further investigate the reaction kinetics of Zn^{2+} in the CaMnO/Zn and $\delta\text{-MnO}_2/\text{Zn}$ batteries. After two activation cycles, GITT analysis was performed on the stable CaMnO and

$\delta\text{-MnO}_2$ samples (Figure 6a). The calculation results of the ionic diffusion efficiency for the two samples are shown in Figure 6b,c. Both samples showed lower ionic diffusion efficiencies at the end of the charging/discharging stage, indicating that the complete insertion and extraction of Zn ions, accompanied by changes in lattice parameters, led to inferior reaction kinetics.^[61] As shown in Figure 6b,c, the diffusion coefficient of the cathode in the first stage ($\approx 1.4 \text{ V}$) was higher than that in the second stage ($\approx 1.1 \text{ V}$), which was related to the insertion reaction of H^+ with a smaller radius in the first discharge platform and the intercalation reaction of Zn^{2+} with a large radius in the second discharge platform.^[26] However, CaMnO exhibits lower electrochemical polarization and higher diffusion coefficient than those of $\delta\text{-MnO}_2$, indicating that the introduction of oxygen vacancies leads to excellent kinetic behavior, which is consistent with the CV results. The Nyquist plots of the prepared electrodes after the first and 100th cycles are displayed in Figure 6d, where the two semicircles represent the EIS impedance (R_{SEI}) in the high-frequency range and the charge transfer impedance (R_{CT}) in the mid-frequency range, and the sloping line is related to the Warburg impedance in the low-frequency region. The two samples showed similar impedance values after the first cycle (Table S3, Supporting Information), but the R_{CT} value of CaMnO only slightly increased from 158.7 to 237.3 Ω after 100 cycles, whereas the impedance of $\delta\text{-MnO}_2$ significantly increased (from 165.2 to 626.8 Ω) after 100 cycles. The lower charge transfer impedance of CaMnO was matched by its higher ionic transfer efficiency and excellent rate capability. These high ion diffusion kinetics and low charge transfer impedance are attributed to the introduction of Ca ions as pillars and the increase in the oxygen vacancy concentration, which

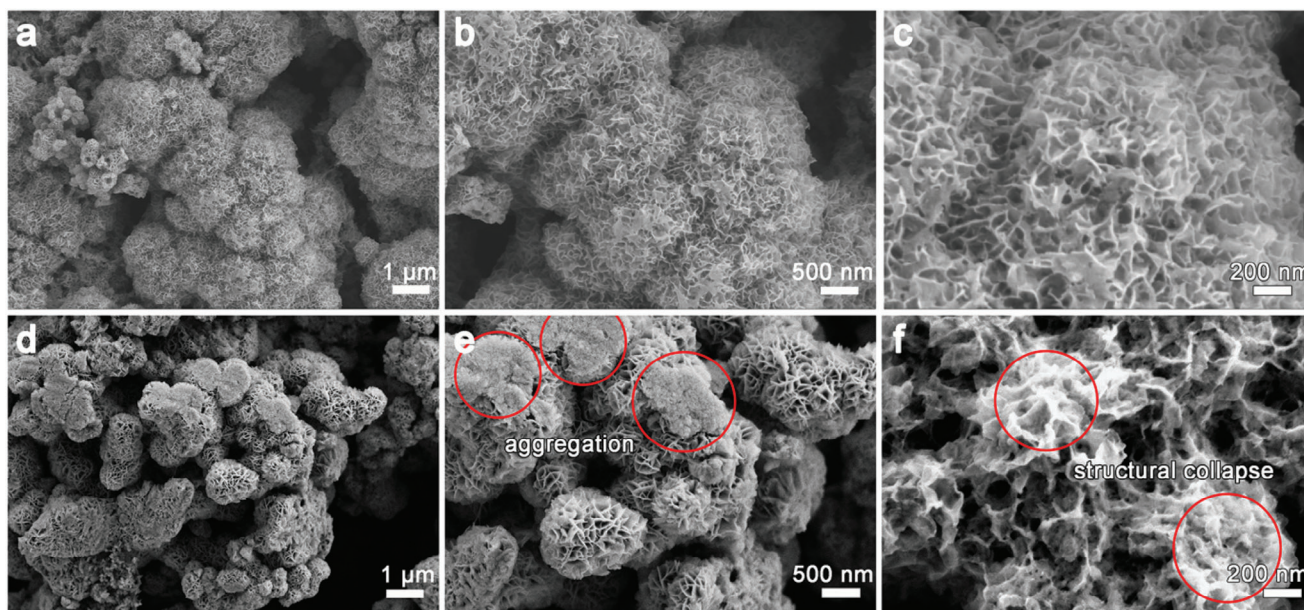


Figure 7. SEM images of (a–c) CaMnO electrode and (d–f) δ -MnO₂ electrode after 50 cycles at 300 mA g⁻¹.

provides the possibility of designing cathode materials with excellent Zn storage performance.

SEM measurements were conducted on the electrodes after 50 cycles at 300 mA h g⁻¹ to further verify the effect of Ca ion doping on structural integrity. The cycled CaMnO material still maintains its original uniformly dispersed nanoflower structure, as shown in **Figure 7a–c**. In contrast, the cycled δ -MnO₂ electrode exhibits significant aggregation and structural collapse (**Figure 7d–f**). The improved structural integrity is related to the introduction of Ca ions as pillars, which enhances the lattice oxygen stability, hinders interlayer slip, and alleviates the lattice parameter changes caused by the insertion of Zn ions. In addition, the improved cycling stability of the cathode material originates from the strong adhesion provided by the modified binders, as discussed in our previous paper.^[62] As shown in **Figure S11** (Supporting Information), the electrode cycled using polyvinylidene fluoride as a binder exhibits significant agglomeration, microcracks, and peeling of the active material, which considerably hinders the electron/ion channels and thus results in poor cyclic stability. Therefore, this optimization strategy for the crystal structure and binder enables the development of high-performance aqueous ZIBs.

Furthermore, the reaction mechanism of the Zn storage process was investigated using ex situ XRD. As shown in **Figure 8a,b**, the (001), (002), (100), (101), (102), and (103) crystal planes of layered MnO₂ can be observed, and the diffraction peak located at 53.1° was assigned to the Ti substrate. During the first discharge platform (discharge to 1.38 V), the characteristic diffraction peak of the (001) and (002) planes of δ -MnO₂ and CaMnO slightly shifted toward higher diffraction angles, but no new phase was formed, which is related to the adjustment of interlayer spacing by H⁺ insertion. Further discharge to 1.25 V can detect the diffraction peak attributed to Zn₂Mn₄O₈·H₂O (JCPDS No. 09–0459), indicating the insertion reaction of Zn²⁺, which is consistent with previous studies.^[63] The diffraction peak attributed to

Zn₄SO₄(OH)₆·5H₂O (JCPDS No. 39–0688) appears at discharge to 1.18 V, and its intensity increases in the deep discharge state, which is attributed to the further insertion of Zn²⁺ and the consumption of H⁺.^[63,64] The new diffraction peaks generated vanished during the charging process, and the intrinsic peak positions of the layered MnO₂ were also well restored, demonstrating excellent structural stability. It is important to note that although most of the characteristic peaks of the two structures overlap, differences between these two materials can still be identified through XRD analysis. For instance, Zn₂Mn₄O₈·H₂O exhibits a high-intensity characteristic peak between 29° and 37°, while the strongest peak of Zn₄SO₄(OH)₆·5H₂O is observed ≈11°. Clearly, the new characteristic peak appeared at 33, 36, and 40° when discharged to ≈1.25 V, while no strong diffraction peak was detected near 11° (**Figure S12**, Supporting Information), indicating that the cathode underwent Zn ion intercalation reaction and formed Zn₂Mn₄O₈·H₂O after the H⁺ intercalation reaction. With further discharge, a strong diffraction peak emerged ≈11°, suggesting the formation of Zn₄SO₄(OH)₆·5H₂O by-products, consistent with previously reported results.^[46] To further demonstrate the reaction product, the TEM spectrum of CaMnO discharged to 1.25 V was analyzed. As shown in **Figure S13** (Supporting Information), numerous crystalline clusters were observed after the insertion reaction. The lattice fringe with distances of 0.225, 0.247, and 0.302 nm correspond to the (004), (211), and (112) plane of Zn₂Mn₄O₈·H₂O, respectively. EDS mapping results reveal a uniform distribution of Mn, Zn, and O elements, with no significant S signal detected, confirming that the reaction product is Zn₂Mn₄O₈·H₂O. In addition, **Figure 8a** shows that the (001) plane moved to a higher angle during the discharge process and recovered during the charging process, which was related to the electrostatic shielding effect caused by cation insertion during discharge, leading to interlayer shrinkage. Compared with δ -MnO₂, the (001) peak of CaMnO underwent a slight increase in peak shift (0.341°) but produced fewer

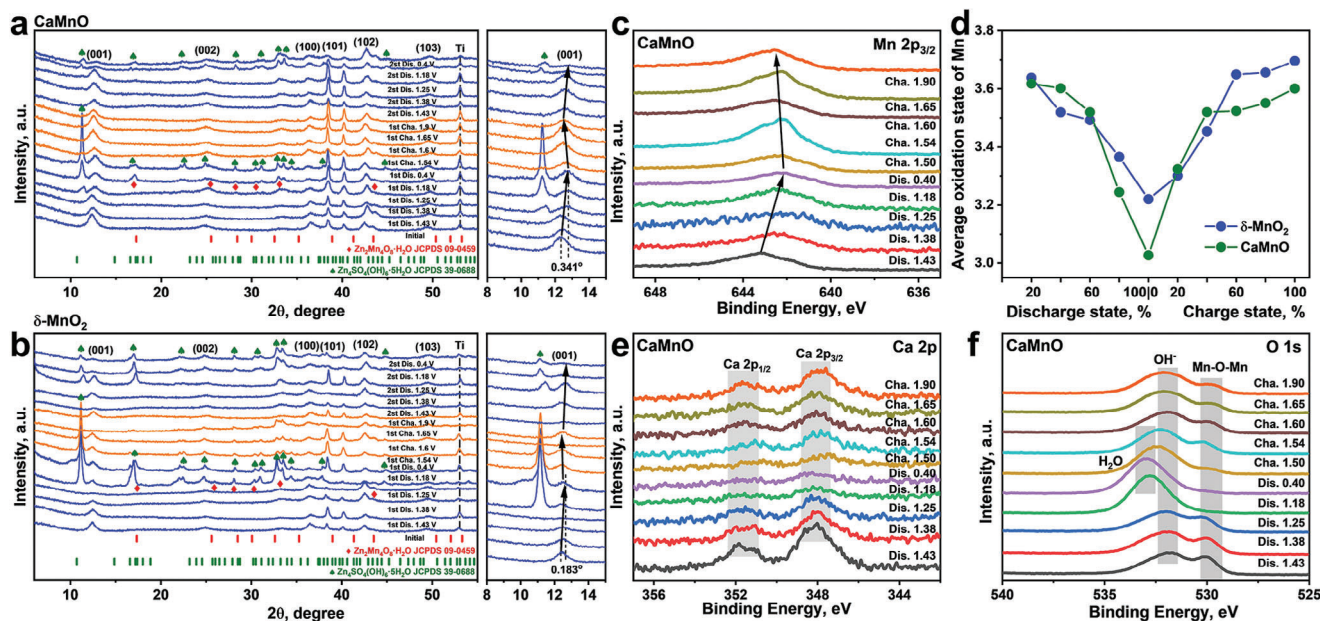


Figure 8. Electrochemical behavior of the synthesized cathode materials. Ex situ XRD patterns of (a) CaMnO and (b) δ -MnO₂ under different state-of-charge ranges during the first discharge and second charge/discharge cycles at 300 mA g⁻¹. c) Mn 2p XPS spectra of CaMnO cathodes under different states of charge, d) and the corresponding average oxidation state of Mn ions. e) Ca 2p XPS spectra of the CaMnO cathode under different states of charge. f) O 1s XPS spectra of the CaMnO cathode under different states of charge.

Zn₄SO₄(OH)₆·5H₂O byproducts, indicating that the introduction of Ca²⁺ alleviated the structural degradation and suppressed the side reactions (Figure 8b). The improved structural stability and reversibility correspond to the enhanced cyclic stability.

As shown in Figure 8c–f, ex situ XPS measurements were conducted to further analyze the charge storage mechanism in the electrochemical processes. As shown in Figure S14 (Supporting Information), characteristic peak signals attributed to the Zn 2p spectrum at 1022 and 1044 eV were detected during the electrochemical process for CaMnO and δ -MnO₂, indicating the intercalation reaction of Zn ions. During the discharge process, the insertion of Zn ions and the formation of zinc sulfate hydroxide hydrate (ZSH) led to a decrease in the intensity of the characteristic peak, whereas the intensity of the characteristic peak gradually decreased during the charging process (reverse process). However, the characteristic peaks related to Zn ions were still detected in the fully charged state, indicating the presence of residual Zn²⁺ in the lattice. The valence states of Mn under different charge states were analyzed using ex situ high-resolution Mn 2p spectroscopy. As shown in Figure 8c and Figure S15a (Supporting Information), the characteristic peak position of Mn 2p_{3/2} gradually shifted toward a lower angle during the discharge process and recovered after charging, confirming the reversible Mn^{3+/4+} redox reaction caused by Zn-ion insertion. Specifically, the average oxidation state of Mn in CaMnO decreases from 3.63 V (original state) to 3.03 V (fully discharge state), which is higher than the value of δ -MnO₂ (from 3.64 to 3.22 V), corresponding to the high reversible capacity caused by the improvement of electronic/ionic conductivity (Figure 8d). In terms of the high-resolution Ca 2p spectra (Figure 8e), a characteristic peak attributed to Ca was observed in CaMnO, and the intensity of this characteristic peak decreased when discharged to 1.18 V and gradually increased af-

ter charging to 1.54 V, indicating binding between Ca²⁺ and the inserted H⁺/Zn²⁺ ions. In addition, in the discharged state, the O 2p spectrum shows a characteristic peak belonging to ZSH at 531.8 eV, which is consistent with the ex situ XRD results, proving the intercalation of hydrated Zn ions (Figure 8f).^[65,66] With further discharge to 1.18 V, the diffraction peak attributed to the newly formed product (Zn₄SO₄(OH)₆·5H₂O) with more crystalline water appeared at 532.9 eV and disappeared when charged to 1.54 V. This result is consistent with the ex situ XRD analysis, demonstrating the high reaction reversibility of CaMnO. On the contrary, crystal water signals can still be detected in fully charged δ -MnO₂, indicating the formation of byproducts containing crystal water and irreversible electrochemical behavior (Figure S15b, Supporting Information). Thus, the introduction of dual-functional Ca ions can effectively enhance the structural stability and reversibility of layered cathodes, which plays a crucial role in improving Zn storage performance.

3. Conclusion

A nanoflower-like CaMnO cathode for aqueous ZIBs was synthesized through a simple, one-step hydrothermal reaction. Introducing Ca ions into layered δ -MnO₂ not only enhances structural stability through a pillar effect but also accelerates Zn-ion diffusion efficiency by expanding the interlayer spacing and introducing oxygen vacancies. Therefore, the optimized cathode exhibited a high reversible capacity and cycling stability, maintaining a reversible capacity of 260 mAh g⁻¹ after 100 cycles at 300 mA g⁻¹ (capacity retention rate of 99%) and achieving a high capacity retention of 80% after 1000 cycles at a high current density of 1500 mA g⁻¹, which is superior to the values reported in the literature. This modification strategy can be easily applied to other

layered Mn-based materials, providing a new perspective for the development of high-performance cathode materials for aqueous ZIBs.

4. Experimental Section

Synthesis of Ca Doped δ -MnO₂ (CaMnO) Cathode: CaMnO was synthesized via a simple hydrothermal reaction. First, CaCl₂ and MnSO₄ were dissolved in deionized water at a molar ratio of 1:1, and KMnO₄ was added at a molar ratio of 6 and stirred for 40 min to obtain a mixed solution. Subsequently, the above solution was transferred to a 50 mL reactor and heated at 160 °C for 12 h. Finally, the solution was centrifuged, washed three times with deionized water, and dried at 60 °C in a vacuum to obtain the final product. For comparison, pure δ -MnO₂ was also prepared through the same process without adding CaCl₂. For comparison, the concentration of Ca doping can be adjusted by varying the ratio of CaCl₂ to MnSO₄ in the solution. The modified samples with CaCl₂ and MnSO₄ ratios of 0.25:1, 0.5:1, 1:1 (experimental group), 2:1, and 4:1 were labeled as CaMnO (0.25:1), CaMnO (0.5:1), CaMnO (1:1), CaMnO (2:1), and CaMnO (4:1), respectively.

Material Characterization: The crystal structure of the samples was measured using XRD (Rigaku Ultima IV with Cu K α radiation) at a sweep speed of 2° min⁻¹ and an angular range of 5°–90°. The morphology of the resulting samples was examined using field-emission scanning electron microscopy (SEM, ZEISS Gemini 300) and high-resolution transmission electron microscopy (HR-TEM, JEOL-2100F). Elemental analysis was performed using XPS (Axis Ultra DLD). Raman spectra were obtained using a Horiba XploRE Raman spectrometer. Desorption tests were conducted using a Micromeritics ASAP 2460 instrument (USA). The precise chemical formula of CaMnO was determined using inductively coupled plasma-optical emission spectroscopy (ICP-OES) (ICAP7400, Thermo Fisher Scientific).

Electrochemical Measurement: An alginate hydrogel binder (Ca-SA) was prepared using previously reported preparation methods.^[62] The electrodes used for electrochemical testing were prepared using traditional casting methods. Typically, CaMnO, carbon black, and alginate hydrogel binder with a weight ratio of 7:2:1 were mixed in deionized water to form a homogeneous slurry, followed by coating on a titanium foil and drying in a vacuum oven at 80 °C for 24 h. Zn foil was used as the anode, a 3 M Zn(CF₃SO₃)₂ aqueous solution as the electrolyte, and glass fiber as the separator. The anode used in the full cell was pre-zincified activated carbon cloth (ACC), rather than Zn foil. First, ACC and Zn foil were assembled into a half-cell. Zn was then electrodeposited onto the ACC to a capacity \approx 1.5 times that of the cathode. Finally, the battery was disassembled to obtain the pre-zincified ACC anode.^[67] Electrochemical measurements were performed using 2032-type coin cells at room temperature. Galvanostatic charge–discharge tests were conducted on a NEWARE auto-cycler in a voltage range of 0.4–1.9 V. Cyclic voltammetry (CV) and electrochemical impedance spectroscopy (EIS) measurements were performed on a CHI 760E electrochemical station. EIS was performed at an open-circuit voltage with an amplitude of 5 mV and a frequency range of 0.01–1 MHz. The Zn ion diffusion coefficient and reaction kinetics of the cathode material were evaluated using CV and GITT. The GITT measurement was conducted by successively applying a current pulse of 90 mA g⁻¹ for 600 s (τ), followed by a 2 h relaxation period to allow the voltage to reach equilibrium. The Zn²⁺ diffusion coefficient (D) is assumed to follow Fick's second law of diffusion. The diffusion coefficient in the single-phase regions can be calculated using the following equation:^[46,61]

$$D = \frac{4}{\pi \tau} \left(\frac{m_B V_M}{M_B S} \right)^2 \left(\frac{\Delta E_S}{\Delta E_r} \right)^2 \quad (1)$$

where m_B , V_M , M_B , S , and τ represent the mass of the active material, the molar volume, the molecular weight of the electrode material, the active surface area, and the duration of the applied current, respectively. ΔE_S and ΔE_r correspond to the differences between the steady-state voltages and

the total transient voltage differences at time τ , which can be calculated from the GITT curve using the method outlined in the current step.

Supporting Information

Supporting Information is available from the Wiley Online Library or from the author.

Acknowledgements

D.X. and Y.W. contributed equally to this work. This study was supported by the National Research Foundation of Korea and funded by the Korean Government (2021R1A2C2011050). Y.W. acknowledges financial support from the Shanghai University of Engineering Science. J.M. acknowledges the funding support from the Australian Research Council Discovery Project (DP240102353).

Conflict of Interest

The authors declare no conflict of interest.

Data Availability Statement

The data that support the findings of this study are available from the corresponding author upon reasonable request.

Keywords

Ca doping, cathode materials, long-term cycling stability, zinc-ion battery, δ -MnO₂

Received: August 2, 2024
Revised: September 15, 2024
Published online: October 3, 2024

- [1] C. D. Quilty, D. Wu, W. Li, D. C. Bock, L. Wang, L. M. Housel, A. Abraham, K. J. Takeuchi, A. C. Marschilok, E. S. Takeuchi, *Chem. Rev.* **2023**, *123*, 1327.
- [2] L. Miao, Y. Lv, D. Zhu, L. Li, L. Gan, M. Liu, *Chin. Chem. Lett.* **2023**, *34*, 107784.
- [3] G. Li, L. Sun, S. Zhang, C. Zhang, H. Jin, K. Davey, G. Liang, S. Liu, J. Mao, Z. Guo, *Adv. Funct. Mater.* **2024**, *34*, 2301291.
- [4] S. Liu, J. Mao, W. K. Pang, J. Vongsivut, X. Zeng, L. Thomsen, Y. Wang, J. Liu, D. Li, Z. Guo, *Adv. Funct. Mater.* **2021**, *31*, 2104281.
- [5] B. Yong, D. Ma, Y. Wang, H. Mi, C. He, P. Zhang, *Adv. Energy Mater.* **2020**, *10*, 2002354.
- [6] X. Zeng, J. Liu, J. Mao, J. Hao, Z. Wang, S. Zhou, C. D. Ling, Z. Guo, *Adv. Energy Mater.* **2020**, *10*, 1904163.
- [7] H. Yaghoobnejad Asl, A. Manthiram, *J. Am. Chem. Soc.* **2020**, *142*, 21122.
- [8] X. Liang, H. Kim, H. G. Jung, Y. K. Sun, *Adv. Funct. Mater.* **2021**, *31*, 2008569.
- [9] H. Li, L. Ma, C. Han, Z. Wang, Z. Liu, Z. Tang, C. Zhi, *Nano Energy* **2019**, *62*, 550.
- [10] T. C. Li, D. L. Fang, J. T. Zhang, M. E. Pam, Z. Y. Leong, J. Z. Yu, X. L. Li, D. Yan, H. Y. Yang, *J. Mater. Chem. A* **2021**, *9*, 6013.
- [11] Q. Ma, Z. Chen, S. Zhong, J. Meng, F. Lai, Z. Li, C. Cheng, L. Zhang, T. Liu, *Nano Energy* **2021**, *81*, 105622.

- [12] Y. B. Li, J. Fu, C. Zhong, T. P. Wu, Z. W. Chen, W. B. Hu, K. Amine, J. Lu, *Adv. Energy Mater.* **2019**, *9*, 1802605.
- [13] D. Selvakumaran, A. Pan, S. Liang, G. Cao, *J. Mater. Chem. A* **2019**, *7*, 18209.
- [14] X. Zeng, J. Hao, Z. Wang, J. Mao, Z. Guo, *Energy Storage Mater.* **2019**, *20*, 410.
- [15] H. He, H. Tong, X. Song, X. Song, J. Liu, *J. Mater. Chem. A* **2020**, *8*, 7836.
- [16] X. Xu, K. Guo, J. Sun, X. Yu, X. Miao, W. Lu, L. Jiao, *Adv. Funct. Mater.* **2024**, *34*, 2400397.
- [17] J. Li, N. Luo, L. Kang, F. Zhao, Y. Jiao, T. J. Macdonald, M. Wang, I. P. Parkin, P. R. Shearing, D. J. L. Brett, G. Chai, G. He, *Adv. Energy Mater.* **2022**, *12*, 2201840.
- [18] V. Mathew, B. Sambandam, S. Kim, S. Kim, S. Park, S. Lee, M. H. Alfaruqi, V. Soundharajan, S. Islam, D. Y. Putro, J.-Y. Hwang, Y.-K. Sun, J. Kim, *ACS Energy Lett.* **2020**, *5*, 2376.
- [19] T. Xiong, Z. G. Yu, H. Wu, Y. Du, Q. Xie, J. Chen, Y. W. Zhang, S. J. Pennycook, W. S. V. Lee, J. Xue, *Adv. Energy Mater.* **2019**, *9*, 1803815.
- [20] X. Cui, Y. Li, Y. Zhang, Z. Sun, Y. Liu, J. Zhang, E. Xie, J. Fu, *Chem. Eng. J.* **2023**, *478*, 147197.
- [21] Q. Song, S. Zhou, S. Wang, S. Li, L. Xu, J. Qiu, *Chem. Eng. J.* **2023**, *461*, 142033.
- [22] J. J. Ye, P. H. Li, H. R. Zhang, Z. Y. Song, T. Fan, W. Zhang, J. Tian, T. Huang, Y. Qian, Z. Hou, N. Shpigel, L. F. Chen, S. X. Dou, *Adv. Funct. Mater.* **2023**, *33*, 2305659.
- [23] W. Yang, L. Dong, W. Yang, C. Xu, G. Shao, G. Wang, *Small Methods* **2020**, *4*, 1900670.
- [24] Y. Fu, X. Gao, D. Zha, J. Zhu, X. Ouyang, X. Wang, *J. Mater. Chem. A* **2018**, *6*, 1601.
- [25] M. Han, J. Huang, S. Liang, L. Shan, X. Xie, Z. Yi, Y. Wang, S. Guo, J. Zhou, *iScience* **2020**, *23*, 100797.
- [26] Y. Wang, Y. Zhang, G. Gao, Y. Fan, R. Wang, J. Feng, L. Yang, A. Meng, J. Zhao, Z. Li, *Nano-Micro Lett.* **2023**, *15*, 219.
- [27] H. Zhang, J. Wang, Q. Liu, W. He, Z. Lai, X. Zhang, M. Yu, Y. Tong, X. Lu, *Energy Storage Mater.* **2019**, *21*, 154.
- [28] M. Xie, M. Lin, C. Feng, Z. Liu, Y. Xu, N. Wang, X. Zhang, Y. Jiao, J. Chen, *J. Colloid Interface Sci.* **2023**, *645*, 400.
- [29] J. Xu, J. Wan, W. Zhang, Y. Li, F. Cheng, Z. Cheng, Y. Xu, S. Sun, Q. Li, C. Fang, *Adv. Funct. Mater.* **2023**, *33*, 2214613.
- [30] M. S. Chae, A. Chakraborty, S. Kunnikuruvan, R. Attias, S. Maddukuri, Y. Gofer, D. T. Major, D. Aurbach, *Adv. Energy Mater.* **2020**, *10*, 2002077.
- [31] N. Zhang, F. Cheng, J. Liu, L. Wang, X. Long, X. Liu, F. Li, J. Chen, *Nat. Commun.* **2017**, *8*, 405.
- [32] C. Zuo, F. Xiong, J. Wang, Y. An, L. Zhang, Q. An, *Adv. Funct. Mater.* **2022**, *32*, 202202975.
- [33] F. Ming, H. Liang, Y. Lei, S. Kandambeth, M. Eddaoudi, H. N. Alshareef, *ACS Energy Lett.* **2018**, *3*, 2602.
- [34] J. Liu, L. Yu, E. Hu, B. S. Guiton, X. Q. Yang, K. Page, *Inorg. Chem.* **2018**, *57*, 6873.
- [35] C. Dong, Z. Qu, X. Jiang, Y. Ren, *J. Hazard. Mater.* **2020**, *391*, 122181.
- [36] C. Xia, J. Guo, P. Li, X. Zhang, H. N. Alshareef, *Angew. Chem., Int. Ed.* **2018**, *57*, 3943.
- [37] Y. Jiao, L. Kang, J. Berry-Gair, K. Mccoll, J. Li, H. Dong, H. Jiang, R. Wang, F. Corà, D. J. L. Brett, G. He, I. P. Parkin, *J. Mater. Chem. A* **2020**, *8*, 22075.
- [38] Y. Wu, Y. Liu, W. Wang, J. Wang, C. Zhang, Z. Wu, P. Yan, K. Li, *J. Mater. Sci.: Mater. Electron.* **2018**, *30*, 842.
- [39] C. Julien, M. Massot, R. Baddour-Hadjean, S. Franger, S. Bach, J. P. Pereira-Ramos, *Solid State Ionics* **2003**, *159*, 345.
- [40] T. Wang, J. Jin, X. Zhao, X. Qu, L. Jiao, Y. Liu, *Angew. Chem., Int. Ed.* **2024**, 202412057.
- [41] Y. Zhang, S. Deng, G. Pan, H. Zhang, B. Liu, X. L. Wang, X. Zheng, Q. Liu, X. Wang, X. Xia, J. Tu, *Small Methods* **2020**, *4*, 201900828.
- [42] M. Zhang, W. Wu, J. Luo, H. Zhang, J. Liu, X. Liu, Y. Yang, X. Lu, *J. Mater. Chem. A* **2020**, *8*, 11642.
- [43] Y. Ma, M. Xu, R. Liu, H. Xiao, Y. Liu, X. Wang, Y. Huang, G. Yuan, *Energy Storage Mater.* **2022**, *48*, 212.
- [44] V. Soundharajan, B. Sambandam, S. Kim, S. Islam, J. Jo, S. Kim, V. Mathew, Y.-K. Sun, J. Kim, *Energy Storage Mater.* **2020**, *28*, 407.
- [45] H. Huang, D. Xie, J. Zhao, P. Rao, W. M. Choi, K. Davey, J. Mao, *Adv. Energy Mater.* **2022**, *12*, 2202419.
- [46] C. Huang, C. Wu, Z. Zhang, Y. Xie, Y. Li, C. Yang, H. Wang, *Front. Mater. Sci.* **2021**, *15*, 202.
- [47] M. H. Alfaruqi, J. Gim, S. Kim, J. Song, D. T. Pham, J. Jo, Z. Xiu, V. Mathew, J. Kim, *Electrochem. Commun.* **2015**, *60*, 121.
- [48] C. Wang, Y. Zeng, X. Xiao, S. Wu, G. Zhong, K. Xu, Z. Wei, W. Su, X. Lu, *J. Energy Chem.* **2020**, *43*, 182.
- [49] F. Wu, Y. Wang, P. Ruan, X. Niu, D. Zheng, X. Xu, X. Gao, Y. Cai, W. Liu, W. Shi, X. Cao, *Mater. Today Energy* **2021**, *21*, 100842.
- [50] Q. Gou, H. Luo, Y. Zheng, Q. Zhang, C. Li, J. Wang, O. Odunmbaku, J. Zheng, J. Xue, K. Sun, M. Li, *Small* **2022**, *18*, <https://doi.org/10.1002/sml.202201732>.
- [51] N. Zhang, F. Cheng, Y. Liu, Q. Zhao, K. Lei, C. Chen, X. Liu, J. Chen, *J. Am. Chem. Soc.* **2016**, *138*, 12894.
- [52] J. Wang, J. Wang, H. Liu, Z. You, Z. Li, F. Kang, B. Wei, *Adv. Funct. Mater.* **2020**, *31*, <https://doi.org/10.1002/adfm.202007397>.
- [53] F. Jing, Y. Liu, Y. Shang, C. Lv, L. Xu, J. Pei, J. Liu, G. Chen, C. Yan, *Energy Storage Mater.* **2022**, *49*, 164.
- [54] S. Zhang, S. Li, H. Zhang, D. Wen, S. Zhang, L. Li, Z. Liu, *Chem. Commun.* **2022**, *58*, 8089.
- [55] J. Guo, J. Ming, Y. Lei, W. Zhang, C. Xia, Y. Cui, H. N. Alshareef, *ACS Energy Lett.* **2019**, *4*, 2776.
- [56] X. Wang, B. Xi, X. Ma, Z. Feng, Y. Jia, J. Feng, Y. Qian, S. Xiong, *Nano Lett.* **2020**, *20*, 2899.
- [57] M. Chen, Q. Cheng, Y. Qian, J. He, X. Dong, *Electrochim. Acta* **2020**, *342*, 136046.
- [58] Y. Qian, C. Meng, J. He, X. Dong, *J. Power Sources* **2020**, *480*, 228871.
- [59] X. Liang, Y. K. Sun, *Adv. Funct. Mater.* **2022**, *32*, 2206154.
- [60] V. Augustyn, P. Simon, B. Dunn, *Energy Environ. Sci.* **2014**, *7*, 1597.
- [61] X. Liang, T.-Y. Yu, H.-H. Ryu, Y.-K. Sun, *Energy Storage Mater.* **2022**, *47*, 515.
- [62] D. Xie, J. Zhao, Q. Jiang, H. Wang, H. Huang, P. Rao, J. Mao, *ChemPhysChem* **2022**, *23*, 202200106.
- [63] W. Zhao, J. Fee, H. Khanna, S. March, N. Nisly, S. J. B. Rubio, C. Cui, Z. Li, L. S. Suib, *J. Mater. Chem. A* **2022**, *10*, 6762.
- [64] C. Zhu, G. Fang, J. Zhou, J. Guo, Z. Wang, C. Wang, J. Li, Y. Tang, S. Liang, *J. Mater. Chem. A* **2018**, *6*, 9677.
- [65] X. Zhang, F. Xue, X. Sun, T. Hou, Z. Xu, Y. Na, Q. An, Z. Chen, S. Cai, C. Zheng, *Chem. Eng. J.* **2022**, *445*, 136714.
- [66] Z. Li, Y. Wei, Y. Liu, S. Yan, M. Wu, *Adv. Sci.* **2023**, *10*, 2206860.
- [67] M. Wang, J. Ma, Y. Meng, J. Sun, Y. Yuan, M. Chuai, N. Chen, Y. Xu, X. Zheng, Z. Li, W. Chen, *Angew. Chem., Int. Ed.* **2023**, *62*, 202214966.